# Miniature Specimen Assessment of Creep of the Single-Crystal Superalloy LEK 94 in the 1000 °C Temperature Range

G. MÄLZER, R.W. HAYES, T. MACK, and G. EGGELER

The creep behavior of the Ni-base superalloy LEK 94 in the 1000 °C range has been investigated. Miniature tensile specimens were employed, which can be taken out of a thin walled blade or used when only limited amounts of material are available. We show that this miniature test technique yields reasonable creep data, including stress exponents $n$ and apparent activation energies $Q_{app}$. The $n$ values are close to 5 and the $Q_{app}$ values are close to 500 kJ/mole, independent of the crystallographic direction. Creep rates are fastest for samples oriented in the [110] direction, followed by [001] samples. The lowest creep rates are observed for the [111] direction. This difference is related to a difference in resolved shear stresses and in the number of activated crystallographic slip systems. As a striking new result, it was observed that the onset of tertiary creep occurs earlier and rupture strains are significantly smaller in the case of [110] specimens as compared to [100] specimens, while the [111] specimens show an intermediate behavior. These effects are related to the alignment of cast porosity along the axis of primary dendrites. When cast micropores align perpendicular to the axis of the applied tensile stress, the onset of fast tertiary creep occurs early and small rupture strains are observed.

DOI: 10.1007/s11661-006-9007-3

## I. INTRODUCTION

SINGLE-CRYSTAL nickel-base superalloys have been the subject of intensive research over the past three decades. These alloys have microstructures consisting of a high volume fraction (typically on the order of 70 vol pct) of cubes of the ordered $\gamma'$ phase ($L1_2$ structure) separated by thin $\gamma$ channels (fcc). The $\gamma'$ particles typically measure 0.4 to 0.5 $\mu$m along the cube edges.[1,2] Because of their excellent creep resistance at high temperatures, single-crystal nickel-base superalloys are used to make turbine blades for gas turbine engines,[3,4,5] where they operate in the 1000 °C temperature regime. In this temperature range, microstructures are not stable and creep limits the service life of components. Therefore, it is imperative to perform reliable creep tests that yield creep rates and rupture times in the relevant temperature range. It is also important to understand the mechanisms that govern creep deformation and rupture.

There is general interest in small specimen geometries; therefore, we recently developed a miniature creep specimen[6,7,8] in order to investigate the creep strength of thin-walled directionally solidified (DS) turbine blades at temperatures of 1303 K. A detailed description of the sample geometry and the testing procedure has been published elsewhere.[6,7,8] Several creep tests were performed on miniature samples taken from a blade of DS Ni-base superalloy CM247LC. The creep curves obtained in References 6 through 8 look reasonable, but no validation by comparison to standard creep specimens was performed. Our miniature creep test technique[6,7,8] is particularly attractive, because specimens can be taken directly out of thin-walled components. In addition, we are also able to obtain creep specimens from a small amount of single-crystal material in all crystallographic directions. In the present study, we use our miniature creep test technique to study creep of the Ni-base single-crystal superalloy LEK 94 at temperatures between 1253 and 1323 K. We show that our miniature creep technique fails to monitor the very early stages of creep but yields reasonable creep data for accumulated strains exceeding 0.2 pct strain. We use our miniature creep specimen to generate tensile creep data for three crystallographic directions [001], [110], and [111].

One objective of the present study is to analyze the creep data in terms of the shape of individual creep curves, as well as with respect to the stress and temperature dependence of the secondary creep rate, and to compare our results to published data from standard size specimens.

The elementary deformation mechanisms of creep in Ni-base single-crystal superalloys have received considerable attention in the scientific literature, and this especially holds for the low temperature/high stress creep regime.[9–19] Microstructural information on high temperature/low stress creep is less frequent. Here, we summarize microstructural results, which are important for high temperature and low stress creep of single-crystal Ni-base superalloys.

---

G. MÄLZER and G. EGGELER are with the Institut für Werkstoffe, Ruhr-Universität Bochum, D-44780 Bochum, Germany. Contact e-mail: gotthard.maelzer@rub.de R.W. HAYES is with the Institut für Werkstoffe, Ruhr-Universität Bochum and Metals Technology Inc., Northridge, CA 91324, USA. T. MACK is with MTU Aero Engines, D- 80995 München, Germany.

Manuscript submitted June 28, 2006

(1) The microstructures of the as-received Ni-base superalloy single crystals generally contain a low density of dislocations. The dislocation density increases during creep. Dislocation loops squeeze into thin $\gamma$ channels.[10,15,20] This is easy in the early stages of channel filling and becomes more and more difficult as creep strain accumulates and the dislocation density in the $\gamma$ channels increases.[21]

(2) In the 1000 °C temperature range, rafting of the $\gamma'$ phase is rapid. In negative misfit alloys, $\gamma'$ rafts form perpendicular to the direction of the maximum principal stress.[10,22–24]

(3) Before rafting has occurred, dislocations in vertical channels can climb to the corners of $\gamma'$ cubes, where they can annihilate with dislocations of opposite sign from horizontal channels. This represents the dominant dynamic recovery process before rafts have formed.[21,25–27]

(4) When $\gamma'$ rafts have formed, the cutting of $\gamma'$ rafts by two dislocations represents the rate controlling recovery mechanism. Two $\gamma$ channel dislocations with different Burgers vectors jointly shear the $\gamma'$ phase by a combined glide and climb mechanism. They annihilate with two $\gamma$ channel dislocations of opposite signs on the other side of the $\gamma'$ raft.[26–29]

(5) Creep rupture of Ni-based single-crystal superalloys seems to initiate by the formation of microcracks at pre-existing cast voids[30] and proceed by subsequent microcrack growth.[30–32] These damage accumulation processes may well affect tertiary creep of Ni-base single-crystal superalloys.

A second objective of our study is to show that the basic high temperature and low stress deformation mechanisms, which were identified for CMSX-6[20,24–26] and CMSX-4,[27] also operate in LEK 94. We investigate the influence of crystallography on creep and characterize the microstructures of selected creep samples in order to correlate the evolution of microstructure with creep behavior. Finally, we examine the microstructural damage evolution during creep and study the fracture characteristics of selected LEK 94 samples to understand the creep failure in LEK 94.

## II. EXPERIMENTAL PROCEDURE

### A. *Material and Sample Preparation*

LEK 94, the material used in this study, is a new Ni-base superalloy single crystal developed by MTU Aero Engines (München, Germany). Its specific chemical composition is given in Table I. The heat treatment consists of solution annealing followed by aging for 5 hours at 1353 K and 8 hours at 1173 K. The miniature creep specimens were taken from 19-mm-diameter [001] rods and from slabs with the dimensions $165 \times 103 \times 20$ mm. Photographs of the LEK 94 slab, which was investigated in the present study, are shown in Figure 1. Figure 1(a) illustrates that the slab edges are parallel to [001] (longitudinal direction), [110] (long transverse direction), and $[\bar{1}10]$ (short transverse direction). In Figure 1(a), two magnified schematic primary dendrites are drawn on the photograph of the slab. Primary dendrites solidify in the [001] direction, and mean primary and secondary dendrite spacings are near 400 and 50 $\mu$m, respectively. The white circles indicate the position of cast micropores that form in between the secondary dendrite arms and that line up along the growth direction of the primary dendrites.

**Table I. Chemical Composition of the LEK 94 Material Used**

| Elements | Co | Al | Cr | W | Re | Ta | Mo | Ti | Ni |
|---|---|---|---|---|---|---|---|---|---|
| Wt pct | 7.5 | 6.5 | 6.0 | 3.5 | 2.5 | 2.3 | 2.1 | 1.0 | bal |

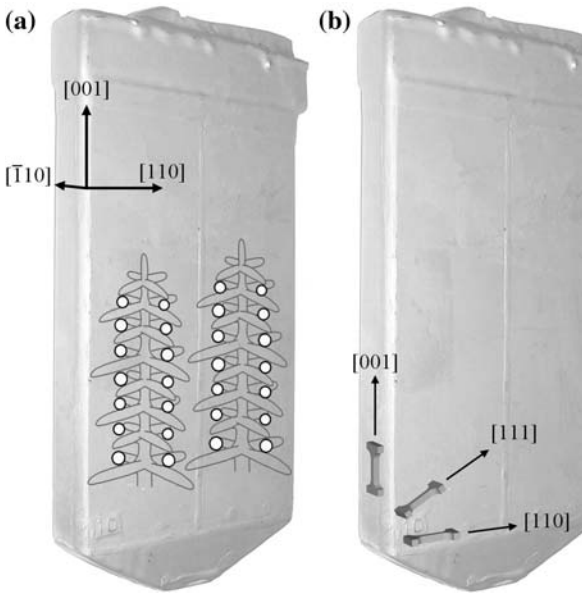

Fig. 1—LEK 94 single-crystal slab used for creep specimen machining. (*a*) Crystallographic directions and schematic illustration of (magnified) dendrites and micropores. (*b*) Three specimen orientations under consideration (photo montage).

The crystallographic orientation of the slab makes it easy to take out miniature creep specimens in [001], [110], and [111] directions. Figure 1(b) represents a montage of the photograph of the slab and pictures of specimens oriented along the three main directions under consideration. An iterative procedure combining the Laue technique to orient the as-received crystals with high precision spark erosion cutting was used to prepare miniature tensile creep specimens in the [001], [100], [110], [101], and [111] directions. The maximum deviation from these directions was 2 deg. Prior to creep testing, all samples were mechanically polished to a mesh size of 2500.

### B. *Creep Testing*

Our miniature creep samples are dog-bone-type specimens with a gage length of 9 mm and a cross section of $2 \times 3$ mm$^2$. Grips for the samples were machined by spark erosion from the oxide-dispersion-strengthened (ODS) alloy PM3030 obtained from Plansee (Reutte, Austria). Creep testing was performed using standard constant load Mayes Mark II TC 20 (Denison Mayes

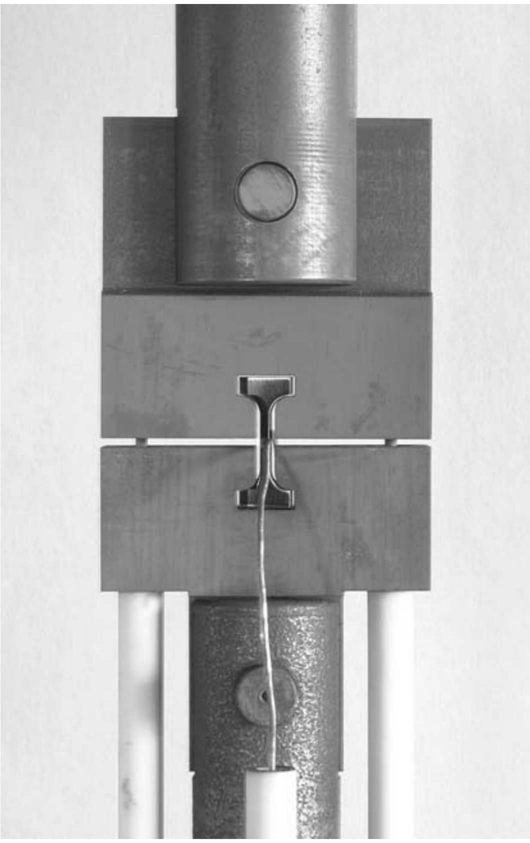

Fig. 2—ODS grips integrate our creep specimen into the load line. Rod in tube extensometers are fixed to the grips and two thermo couples are attached to the specimen.

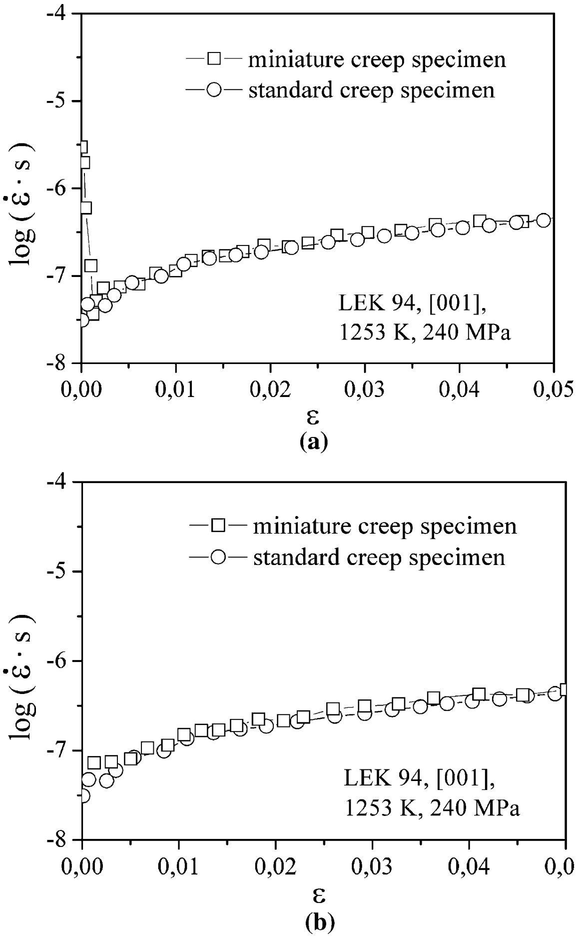

Fig. 3—Creep curves of a standard creep specimen (circles) and of our new miniature creep specimen (squares). The logarithm of creep rate log $\dot{\varepsilon}$ is plotted *vs* strain $\varepsilon$: (*a*) raw data and (*b*) miniature data corrected.

Group, Leeds, United Kingdom) creep machines equipped with furnaces capable of temperatures up to 1200 °C. Figure 2 shows our specimen as integrated in the load line during creep testing. Figure 2 shows the loading bars; the two ODS grips, which transfer the load to the specimen; the outer tubes (attached to the lower ODS grip), which are used for $Al_2O_3$ ceramic rod in tube extensometry; and one of two thermocouples attached to the specimen.

As shown in Figure 2, strains are not directly taken from the gage length of the creep specimens. It was found that at the beginning of creep, the samples adjust to the grips. This leads to an apparent primary creep range that represents an artifact. Figure 3(a) shows two creep curves plotted as a logarithm of creep rate *vs* strain obtained under creep conditions of 1253 K and 240 MPa. A standard creep specimen (with direct strain measurement from the gage length of the specimen) yields creep curves that start at low creep rates, which steadily increase throughout creep (circles in Figure 3(a)). Our miniature creep data (squares in Figure 3(a)) deviate from the data of the standard specimen within the first 0.2 pct of testing. Most importantly, they predict decreasing creep rates that are not actually observed using standard creep specimen geometries. The width of the strain range, where creep rates apparently decrease in the early stages of miniature creep testing, is subtracted from the creep curves of our miniature creep data. Figure 3(b) shows the creep curve of the miniature specimen (squares) after this correction, together with the same standard creep data (circles) as in Figure 3(a).

Creep tests were carried out in uniaxial tension at temperatures ranging from 1253 to 1323 K and stress levels between 160 and 240 MPa in air. Most creep tests were taken through to failure to monitor the entire creep curves and to characterize the fracture mode and the features that lead to failure of LEK 94. For the evaluation of the stress and temperature dependence of creep, creep rates were determined at creep strains of 5 pct. Some creep tests were terminated prior to failure of the sample. These tests were cooled rapidly to room temperature under load in order to preserve the microstructural features during creep for a detailed analysis using transmission electron microscopy (TEM).

### C. *Characterization of Microstructures*

Samples for TEM were taken from selected creep specimens by cutting 0.5-mm-thick slices from the gage section parallel to the specimen axis. Thinning of TEM samples was accomplished using an electrolyte consisting of 70 vol pct methanol, 20 vol pct glycerin, and 10 vol pct perchloric acid at −20 °C. The TEM was performed using a PHILIPS* CM20 operating at 200 kV.

Figure 4 shows a TEM micrograph of the as-received fully heat-treated single-crystal alloy LEK 94 used in this study. The $\gamma$-matrix lattice reflections (strong spots) along with the $\gamma'$-superlattice reflections (weak extra spots) are shown in the corresponding selected area diffraction pattern. The microstructure of this alloy shows the generic features of single-crystal superalloy microstructures, as reported in the literature.[1,2,9,10,20,25] Our alloy contains a high volume fraction of $\gamma'$ cubes precipitated within the $\gamma$ matrix, which forms thin channels separating the cubes. The $\gamma'$ particles measure approximately 0.3 $\mu$m along the cube edges. The initial dislocation density within the thin $\gamma$ matrix channels is very low. Only occasional dislocations such as those highlighted at the $\gamma/\gamma'$ interface (arrows in Figure 4) are observed in the undeformed material.

In addition to TEM, scanning electron microscopy (SEM) was performed on our flat miniature creep samples. Preparation of the samples consisted of grinding, mechanical polishing, and etching. Samples were etched electrolytically (6 V dc) for approximately 3 seconds in a mixture of 12 mL perchloric, 47 mL sulfuric, and 41 mL nitric acid using a procedure described in Reference 33. During etching, a surface topography evolves by selective dissolution of the $\gamma$ phase. Fracture surfaces were cleaned in ethanol prior to SEM examination. Investigations were carried out using a Leo Gemini 1530 operating at an accelerating voltage of 12 kV and a JEOL† JSM 6340 F at 10 kV.

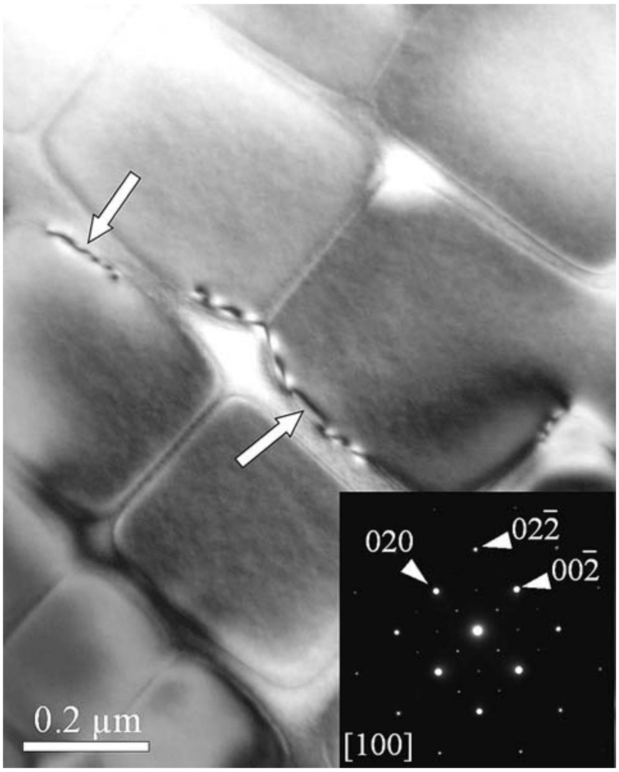

Fig. 4—TEM micrograph of the as-received fully heat-treated LEK 94 single-crystal superalloy showing the $\gamma'$ morphology and corresponding electron diffraction pattern. The arrows mark dislocations in the as-received material (prior to creep).

## III. RESULTS

### A. *Creep Behavior*

The creep response of the single-crystal alloy LEK 94 is shown in Figure 5, where the logarithm of strain rate is plotted against strain for different stresses at 1293 K (Figure 5(a)) and for different temperatures at 200 MPa (Figure 5(b)). Figure 5 represents the creep response of the LEK 94 single-crystal alloy under all creep conditions considered in this study. It can be seen that none of the creep curves exhibit a well-defined steady state or minimum strain rate. Instead, the strain rate slowly and steadily increases toward the termination of the test or failure of the sample. Figure 5 shows that the [001] direction is associated with the largest rupture strains, which exceed those observed for [110] specimens by a factor of 2. Figure 5 also clearly documents that the slope of the $\log \dot{\varepsilon}(\varepsilon)$ curves, which represent the increase of creep rate with strain, is significantly higher for the [110] direction than for the [001] direction. In order to clarify these findings, two additional creep tests were performed. The results are presented in Figure 6. Figure 6(a) shows creep curves for [100] and [001] specimens. The two creep curves show no difference for strains below 10 pct, while the [100] specimen shows an earlier onset of fast tertiary creep (arrow) and a lower rupture strain. Correspondingly, the [101] and [110] specimens have a very similar creep behavior below 10 pct, while the [110] specimen shows an earlier onset of fast tertiary creep (arrow) and fails at lower strains (Figure 6(b)).

Following Kamaraj *et al.*,[25] we take the creep rate at 5 pct strain as a representative strain rate to characterize the stress and temperature dependence of the creep rate. Figure 7 (a) shows the creep rate at 5 pct strain plotted against stress on a double logarithmic scale for all three crystallographic directions at 1293 K. This yields apparent stress exponents close to 5 for the three crystallographic directions (4.6, 5.6, and 5.3 for the [001], [110], and [111] specimens, respectively).

Figure 7(b) shows an Arrhenius plot of the natural logarithm of creep rate as a function of the inverse absolute temperature for experiments performed at a stress of 200 MPa. From Figure 7(b), we obtain apparent activation energies close to 500 kJ/mole for the three crystallographic directions (477 kJ/mole, 531 kJ/mole, and 482 kJ/mole for the [001], [110], and [111] crystallographic directions, respectively).

---

*PHILIPS is a trademark of Philips Electronic Instruments Corp., Mahwah, NJ.

†JEOL is a trademark of Japan Electron Optics Ltd., Tokyo.

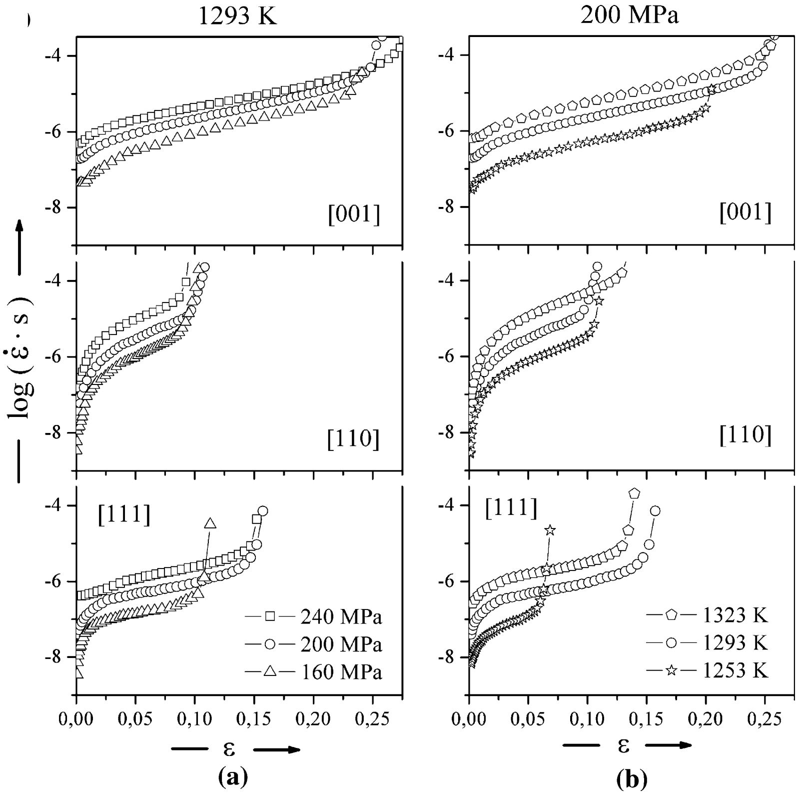

Fig. 5—Creep curves as logarithm of strain rate *vs* strain (log $\dot{\varepsilon}$ *vs* $\varepsilon$) of the superalloy single-crystal LEK 94: (*a*) stress dependence at 1293 K and (*b*) temperature dependence at 200 MPa.

As can be seen from Figures 7(a) and (b), the creep rate at 5 pct strain is highest in the [110] direction followed by the [001] and [111] directions. The [111] specimens show the lowest creep rates (factor 10 slower than [110] data!).

### B. *Microstructural Evolution of Precipitates and Dislocation Substructure*

Under the creep conditions investigated in the present study, rafting always occurs. This is demonstrated for the case of a [001] creep test at 1293 K and 200 MPa in the SEM micrographs of Figure 8. Interrupted tests were taken through to 0.5 pct (12 hours), 1 pct (17.5 hours), and 5 pct (39 hours) strain. LEK 94 is a negative misfit alloy and, therefore, rafting occurs perpendicular to the direction of the applied stress. The SEM contrast in Figure 8 is such that the $\gamma'$ rafts appear bright.

It is interesting to see that in Figures 8(b) and (c), the $\gamma'$ phase almost completely surrounds the $\gamma$ regions. This type of microstructural evolution has been referred to as topological inversion.[34,35] A simple line intersection method was used to obtain preliminary estimates for the widths of the $\gamma$ channels, the thicknesses of $\gamma'$ rafts, and the $\gamma'$-volume fractions.[36] The positions of the reference lines used for the evaluation are indicated in Figures 8(a) through (c). The width of each $\gamma$ channel ($w_i$) and the thickness of each individual $\gamma'$ raft ($t_i$) were measured. Mean $\gamma$ channel $\bar{w}$ and $\gamma'$-raft thicknesses $\bar{t}$ were obtained as

$$\bar{w} = \frac{1}{n} \cdot \sum_{i=1}^{n} w_i \text{ and } \bar{t} = \frac{1}{n} \cdot \sum_{i=1}^{n} t_{\mathrm{i}} \qquad [1]$$

A value for the corresponding $\gamma'$-volume fractions was simply obtained using

$$f_V = \frac{\sum t_i}{\sum w_i + \sum t_i} \qquad [2]$$

Our results for $\bar{w}$, $\bar{t}$, and $f_V$ are presented in Table II. We appreciate that our simple assessment of rafting does not reveal all details of the underlying kinetic processes. However, in agreement with Reference 37, we find that the thickness of the $\gamma'$ rafts as measured with our simple method initially decreases. This is associated with diffusion into and an associated closure of vertical channels, as has been discussed in the literature.[38] A simultaneous steady increase of the width of $\gamma$ channels is also in line with results reported earlier.[37] The initial decrease of $\gamma'$-raft thickness, $\bar{t}$, followed by a subsequent increase of $\gamma$-channel width, $\bar{w}$, is shown in Figure 9 (a). In agreement with what has been reported by Serin *et al.*,[38] there is a decrease of $\gamma'$-volume fraction from values near 80 pct in the initial state to lower values (Figure 9(b)).

Figure 10 shows an SEM micrograph of the $\gamma/\gamma'$ morphology in the undeformed grip section of a sample crept for 57 hours at 1293 K and 200 MPa (the crept part of this creep specimen is shown in Figure 8(c)). A

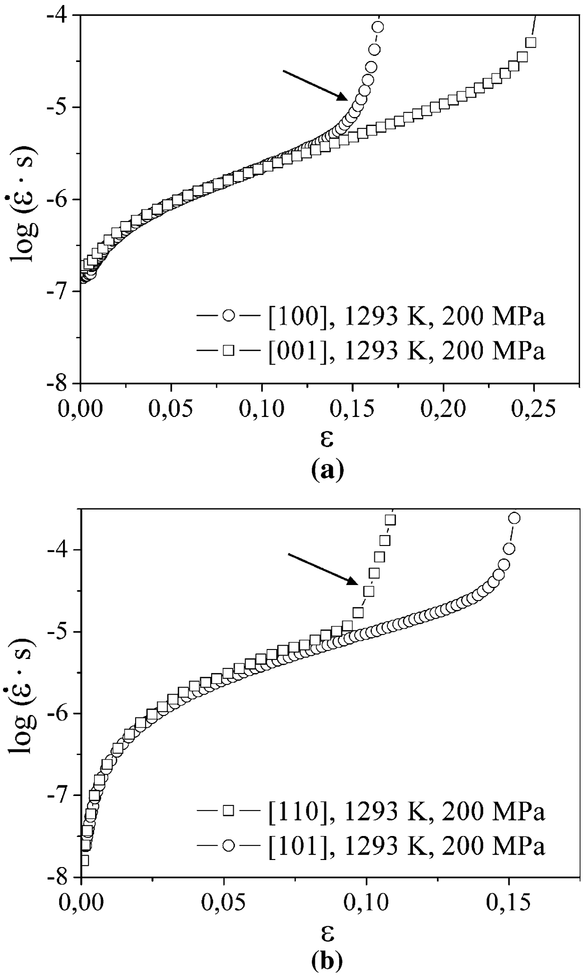

Fig. 6—Creep curves as the logarithm of strain rate *vs* strain (log $\dot{\varepsilon}$ *vs* $\varepsilon$) for two different types of (*a*) < 100 > and (*b*) < 110 > directions.

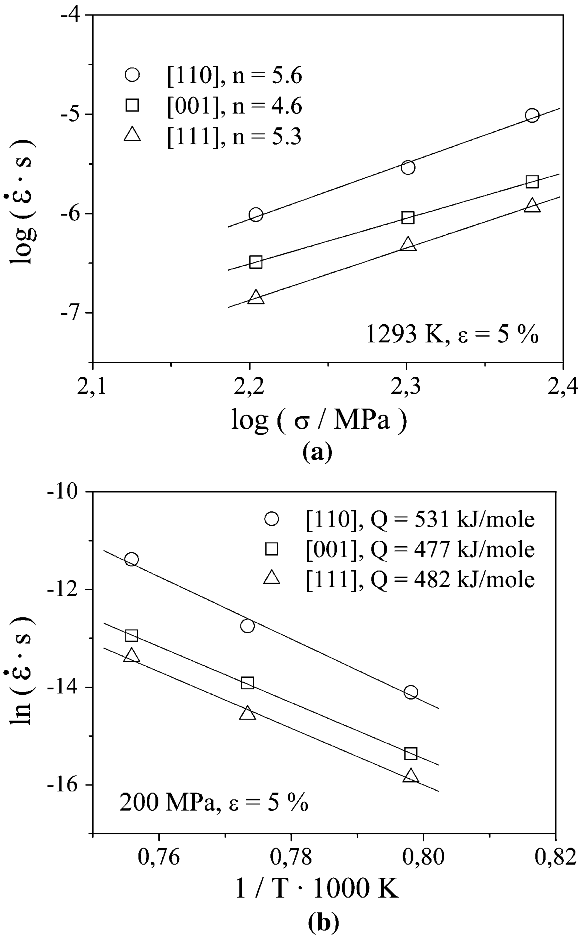

Fig. 7—(*a*) Log-log plot of strain rate *vs* stress yielding stress exponents *n* for the [001], [110], and [111] crystallographic directions at 1293 K. (*b*) Arrhenius plot of natural logarithm of strain rate *vs* $1/T$, yielding apparent activation energies for creep at 200 MPa. Creep rates taken at 5 pct strain.

comparison with the TEM micrograph from Figure 4 suggests that the particles have coarsened. However, in the absence of stress, coarsening is not directional and rafts such as those shown in Figure 8 are not detected. Arrows in Figure 10 indicate the positions of ledges in the $\gamma/\gamma'$ interfaces, which represent the SEM analogous to what Kolbe and co-workers have observed after creep of CMSX-6 using TEM.[39] Kolbe *et al.*[39] suggest that such ledges indicate that dislocations locally interact with the coarsening process. Further work is required to study this phenomenon.

Figure 11 shows two TEM micrographs obtained from a [001] standard creep specimen crept to fracture at 1253 K and 240 MPa. Figure 11(a) documents that there is a high dislocation density in the $\gamma$ channels, while Figure 11(b) provides microstructural evidence for $\gamma'$ cutting. In our material, we observe a cutting mechanism, which was already reported for CMSX-6,[26] CMSX-4,[27] and TMS 138.[29] In this process, two $\gamma$-channel dislocations with different Burgers vectors jointly shear the $\gamma'$ phase. A detailed analysis of this $\gamma'$-cutting process is given elsewhere.[28]

### C. *Cast Porosity and Microcracks*

Figure 12 shows two SEM micrographs taken at a lower (Figure 12(a)) and higher (Figure 12(b)) magnification. In Figure 12, we look onto the rupture surface of a [110] specimen where rupture occurred after 21 hours at 1323 K and 200 MPa. Figure 12(b) illustrates that the microstructural features in Figure 12(a) correspond to dendritic and interdendritic regions. The positions of primary and secondary dendrites are indicated in Figure 12(b). As shown in Figure 1(a), primary dendrites solidify in the [001] direction. Cast micropores are detected between the secondary dendrite arms. Three cast micropores are highlighted by arrows in Figure 12(b). When cast micropores form between the secondary dendrite arms, this results in aligned porosity along the [001] direction (Figure 12(b)). The average secondary dendrite spacing of around 50 $\mu$m is in good agreement with the microstructural data reported by Bouse and Mihalisin.[40]

On rupture surfaces of [001] specimens, this alignment cannot be detected, but individual pores are visible. Figures 13(a) and (b) show the rupture surfaces of

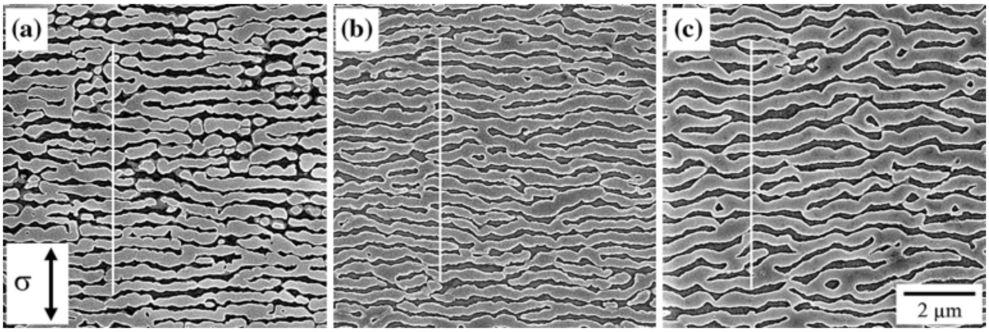

Fig. 8—SEM micrographs showing rafted microstructures after [001] tensile creep testing at 1293 K and 200 MPa taken through to different levels of strain/time: (*a*) 0.5 pct (12 h), (*b*) 1 pct (17.5 h), and (*c*) 5 pct (39 h).

**Table II. Mean $\gamma$-Channel Width, $\bar{w}$, Mean $\gamma'$-Raft Thickness, $\bar{t}$, and Estimated $\gamma'$-Volume Fraction $f_V$ of [001] Specimens; Measurements and Calculations are Achieved along the White Lines in Figures 8(a) through (c)**

| Strain: Compare to: | 0.5 pct (Fig. 8(a)) | 1 pct (Fig. 8(b)) | 5 pct (Fig. 8(c)) |
|---|---|---|---|
| $\bar{w}$($\mu$m) | 0.08 | 0.12 | 0.14 |
| $\bar{t}$ ($\mu$m) | 0.31 | 0.27 | 0.31 |
| $f_V$ (pct) | 79 | 69 | 69 |

specimens that were creep loaded parallel to the direction of the primary dendrites. Terraces appear at different heights, and it is no longer possible to locate dendrite positions. Square-shaped fields can be detected around small cast pores, which can be clearly recognized on the rupture surface of the 1253 K specimen and which loose definition at higher temperature (Figure 13(b)). The directions of the edges of these square fields are of type < 110 >, as indicated in Figure 13(b). These directions are in agreement with those reported by Sherry and Pilkington,[31] who proposed a crystallographic scenario that rationalizes this square geometry.

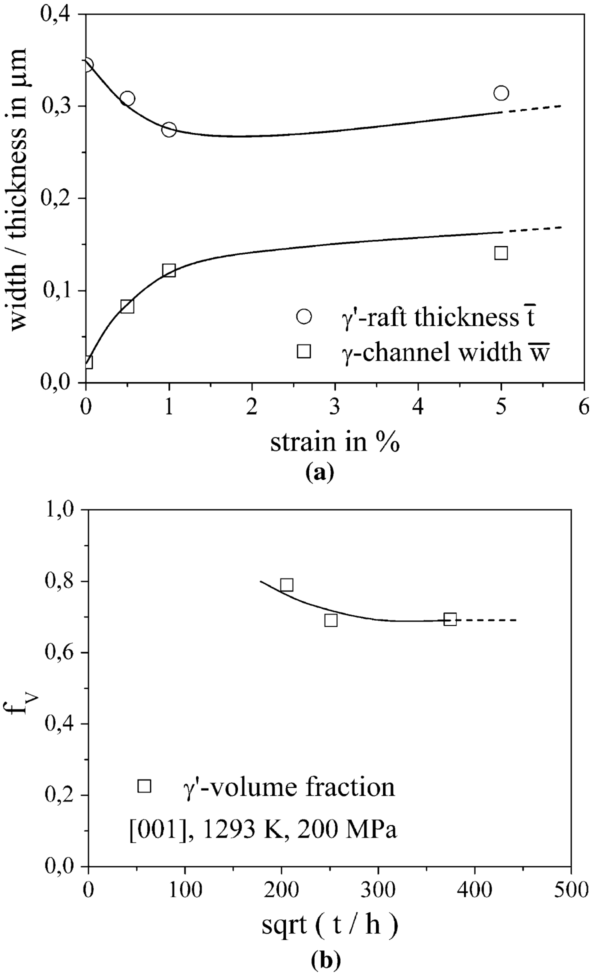

Fig. 9—Evolution of parameters characterizing the $\gamma'$ microstructures from Fig. 8. (*a*) $\gamma$-channel width $\bar{w}$ and $\gamma'$-raft thicknesses $\bar{t}$ as a function of strain. (*b*) $\gamma'$-volume fraction as a function of the square root of time.

When pores are observed in creeping solids, it has to be established whether they nucleate and grow during creep (as in steels and other high temperature alloys[41,42,43]) or whether they are associated with the processing of the material. It is well known that cast micropores can form during solidification.[40] Fine micropores can be detected in the material investigated in the present study prior to creep testing. One example of a pre-existing void is shown in the SEM micrograph taken from a polished cross section of the as-received material (Figure 14 (a)). The pre-existing void shows weak crystallographic features. Long-term annealing in the undeformed head of a creep specimen leads to a sharper definition of the facets in the pore. This is shown for the polished and etched undeformed specimen head of a [001] creep specimen (1293 K, 240 MPa, 25 hours) in the SEM micrograph of Figure 14(b). The pore facets are parallel to {100} and {110} planes. While more work is required to clarify this point, it is clear from Figure 14(a) that cast micropores pre-exist in LEK 94 and do not need to nucleate during creep. From a micromechanical point of view, it is important to highlight that the intersections of pore facets in Figure 14(b) represent micronotches.

Figure 15 shows an SEM micrograph of microcracks that start from a void. The micrograph was taken at a distance of 2 mm from the rupture surface of a specimen that failed after 193 hours at 1293 K and 160 MPa.

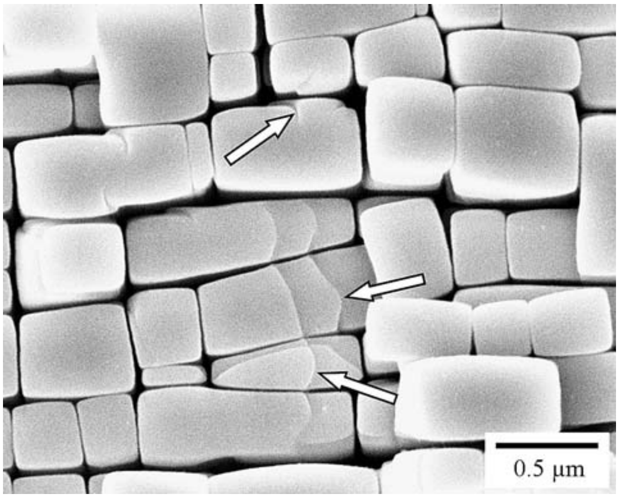

Fig. 10—SEM image from the unstressed head of the [001] sample crept at 1293 K and 200 MPa. The $\gamma'$ phase remains entirely cuboidal in the absence of an externally applied stress. Arrows mark ledges formed during coarsening.

Therefore, the microcracks shown in Figure 15 were not responsible for final rupture. However, Figure 15 sheds light on the later stages of damage accumulation during tertiary creep. Microcrack nucleation occurs near micronotches defined by the intersections of the crystallographic pore facets shown in Figure 14.

In two cases, details of microcrack propagation from pre-existing cast pores could be observed. The SEM micrograph of Figure 16 (a) shows that a microcrack grows toward the right from a pre-existing cast pore. The SEM micrograph of Figure 16(b) was taken at a higher magnification and suggests that the microcrack grows along $\gamma/\gamma'$ interfaces ($\gamma'$ phase: dark, $\gamma$ phase: bright). However, in the same temperature range, we also find evidence for straight cracks that grow perpendicular to the direction of the applied stress and that do not seem to be affected by microstructural features (Figure 17). In fact, the fine straight microcrack in Figure 17(b) propagates directly through a $\gamma'$ raft at a position marked by a white arrow.

## IV. DISCUSSION

### A. *Miniature Creep Testing and Creep Parameters*

The creep data that we obtained for LEK 94 tensile creep in three crystallographic directions are presented in Figures 5 through 7. Our creep test technique does not capture the very early stages of creep ($\varepsilon < 0.2$ pct), but it yields reliable creep data for accumulated strains higher than 0.2 pct. Thus, Figure 3 shows that for creep strains higher than 0.2 pct, our miniature creep test procedure yields the same creep data as a standard creep specimen. Figure 6 demonstrates that in the early stages of creep, where aligned porosity does not yet affect the creep behavior, two crystallographic equivalent directions yield identical creep rates.

For all tests performed in the present study, creep rates steadily increase. In the temperature and stress range investigated, LEK 94 does not show classical steady-state creep. Only a part of the increase in creep rate is associated with constant load creep testing performed in our study.[44] Another part of the increase of the creep rate is due to microstructural softening and damage accumulation processes.

It is interesting to note that the slope of the $\log \dot{\varepsilon}(\varepsilon)$ creep curves of the [110] creep tests is significantly steeper than that of the [001] specimens (Figure 5). Figure 5 also shows that the [110] specimens fail with rupture strains, which are significantly smaller than the

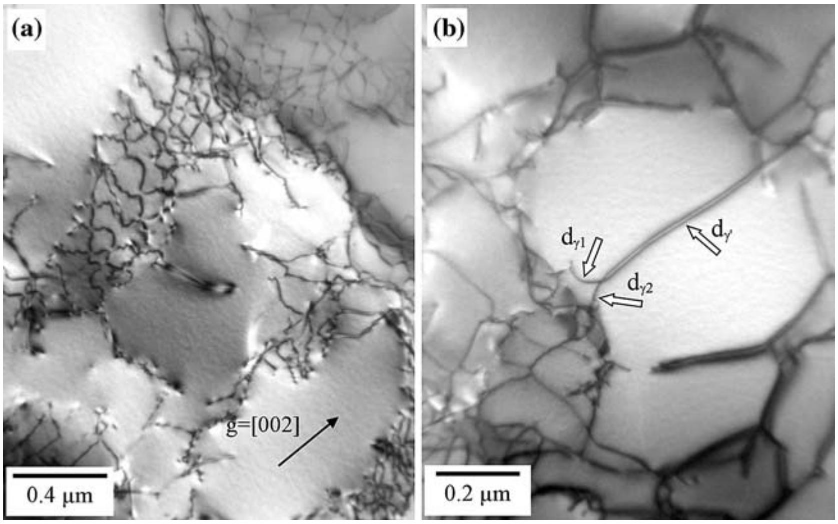

Fig. 11—TEM micrographs of the dislocation structure formed during creep to fracture of a standard creep sample in the [001] direction at 1253 K and 240 MPa. (*a*) High dislocation density in the $\gamma$ phase. (*b*) Cutting of the $\gamma'$ phase: a superdislocation $d_{\gamma'}$ is formed by two $\gamma$-channel dislocations $d_{\gamma 1}$ and $d_{\gamma 2}$ (marked by arrows).

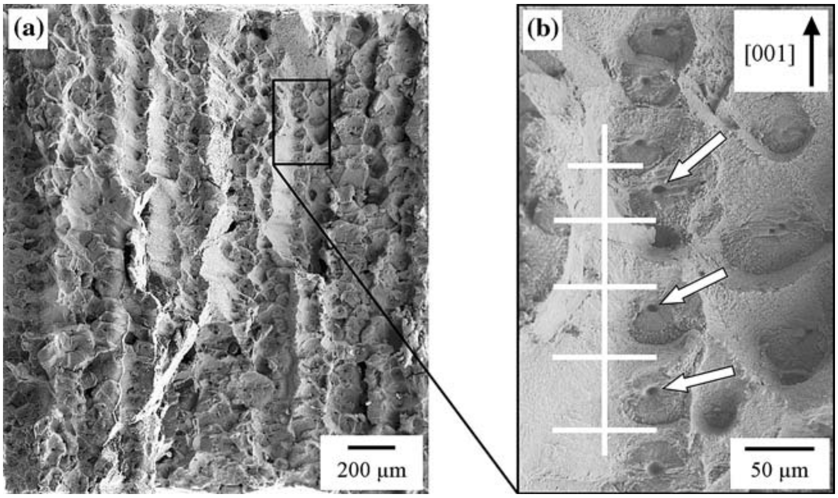

Fig. 12—SEM image of the fracture surface of the [110] sample crept at 1323 K and 200 MPa. (*a*) Overview of the entire surface. (*b*) Marked area at higher magnification. Micropores align along interdendritic regions. Positions of primary and secondary dendrite arms are highlighted.

rupture strains of the [001] specimens. Before we consider this interesting result, in Section B, we first discuss the stress and temperature dependence of creep in terms of the stress exponent $n$ and the apparent activation energy of creep $Q_{\mathrm{app}}$.[45,46] For this purpose, we use creep rate data that were taken at 5 pct strain.

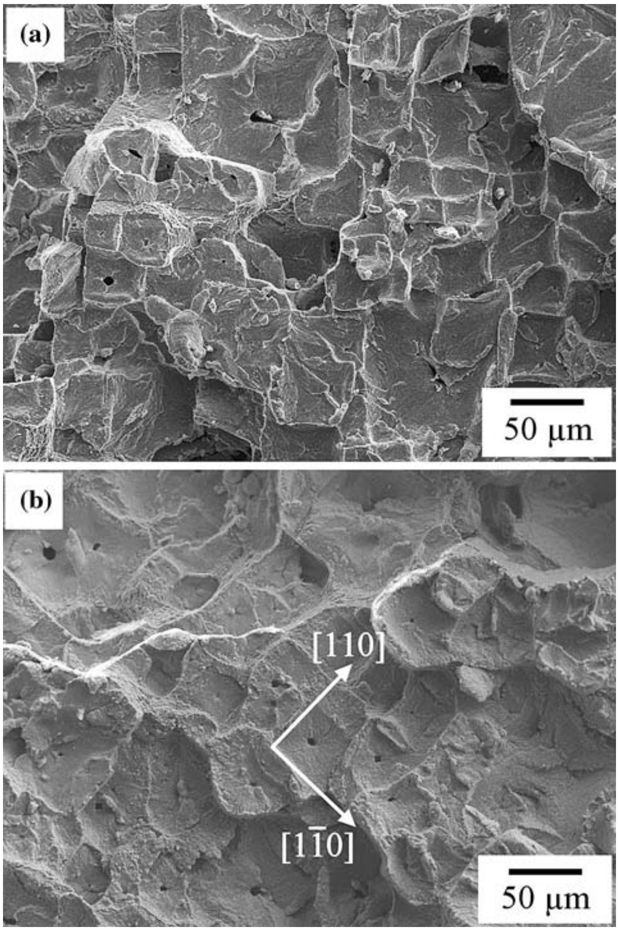

Fig. 13—SEM images of [001] samples crept at (*a*) 1253 K, 240 MPa and (*b*) 1323 K, 200 MPa. The fracture surfaces are comprised of well-defined crystallographic fracture facets. The directions of the edges are indicated by arrows. Small pores are located at the bottom of the facets.

The apparent activation energy $Q_{\mathrm{app}}$ and the stress exponent $n$ are phenomenological parameters that are obtained from the plots presented in Figures 7(a) and (b). We present these values in Table III. It is interesting to note that while there is a clear influence of crystallography on the creep behavior of LEK 94 (different creep rates for different tensile directions, different slopes of $\log \dot{\varepsilon}(\varepsilon)$curves in different tensile directions, differences in the onset of fast tertiary creep, and rupture strains in different tensile directions), this does not seem to strongly affect the stress and temperature dependence of the overall creep process. Values of $Q_{\mathrm{app}}$ and $n$ are always close to 500 kJ/mole and 5, respectively, independent of the tensile direction. In Table III, we compare the results that we obtained in the present study with data that were published in the literature.[10,15,25,37,47–49] It can be seen that apparent activation energies are often found close to 500 kJ/mole, independent of the type of test (tensile creep/shear creep), the crystallographic direction, or the specific Ni-base superalloy. Experimental values for the apparent activation energies of creep of single-crystal superalloys are significantly higher than the values reported for the apparent activation energy of self-diffusion of Ni* in Ni (285 kJ/mole[50]) and in Ni$_3$Al (306 kJ/mole[51]). These data do not allow exclusion of the possibility of creep rates in single-crystal superalloys being governed by simple diffusion-controlled dislocation climb processes. Self-diffusion data of Ni* in $\gamma$ and in $\gamma'$ for the alloy composition investigated in the present study are not available.

Our values for stress exponents $n$ are low as compared to the values that were reported for other superalloy single crystals (Table III). However, they support the general trend that $n$ values decrease with increasing temperatures and decreasing stresses. It is also important to highlight that all experimental values for stress exponents in Ni-base superalloys are higher than 3 or 4

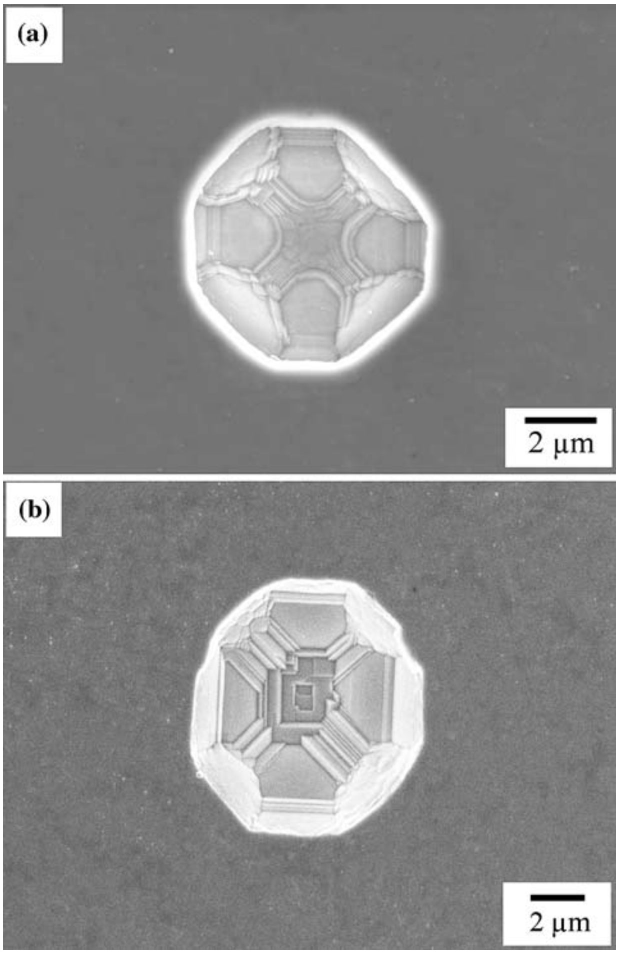

Fig. 14—Facets in a pore: (*a*) initial state and (*b*) head area of a specimen after 25 h at 1293 K.

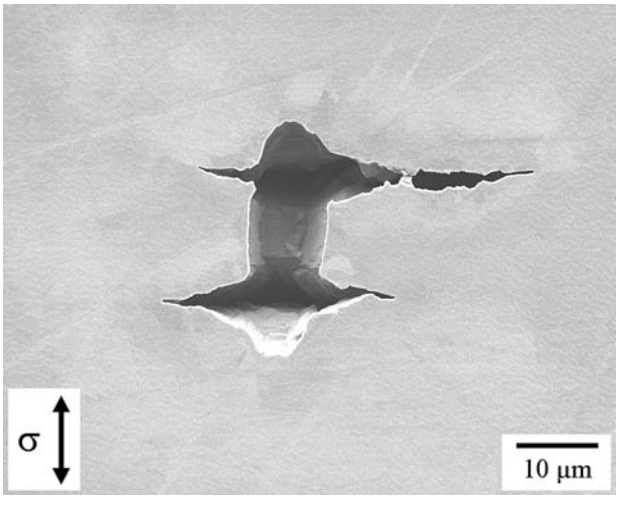

Fig. 15—SEM micrograph from a [001] sample crept at 1293 K and 160 MPa for 193 h (after polishing). Microcracks grow perpendicular to the direction of the applied stress from a vertically elongated pore.

(Table III). Therefore, creep in Ni-base superalloy single crystals cannot be explained assuming natural steady-state laws of creep.[45,46]

### B. *Microstructural Aspects of Creep*

We have shown that creep of the single-crystal superalloy LEK 94 is accompanied by a number of different elementary microstructural processes. These include dislocation plasticity in the $\gamma$ channels (channel filling and formation of networks) and in the $\gamma'$ phase (pairwise cutting), the directional coarsening of the $\gamma'$ phase (rafting), and the formation and growth of microcracks from pre-existing cast voids. Our results on dislocation processes and rafting show that these processes occur in LEK 94 in very much the same way as in several other Ni-base single-crystal superalloys (CMSX-6, CMSX-4, and TMS-138[26,27,29]). These are generic deformation and softening processes that govern the high temperature and low stress creep behavior of the entire family of Ni-base single-crystal superalloys.

The fact that creep rates are fastest in the [110] direction followed by the [001] and [111] directions and that the [111] specimens show the lowest creep rates (a factor of 10 slower than [110] data) can be partly rationalized using a resolved shear stress argument. Three sets of Schmid factors describing the intensities of the resolved shear stresses in the 12 independent crystallographic slip systems of the three types of tensile tests considered in the present study are listed in Table IV. It can be seen that [111] tensile testing, which is associated with the lowest creep rates, shows the lowest Schmid factors (6 out of 12 independent crystallographic <01–1> {111} slip systems have Schmid factors of 0.272, while the Schmid factors of the 6 remaining crystallographic slip systems are 0). The two other tensile creep directions, [001] and [110], both show average Schmid factors of 0.408. However, there are eight crystallographic slip systems in the case of the [001] direction, while only four crystallographic slip systems characterize the loading condition in the case of [110] tensile creep. Our results presented in Figure 6 suggest that early creep is faster for [001] than for [110] tensile creep. This may be related to the fact that more slip systems can contribute to plastic deformation. For higher strains, however, this higher number of slip systems may result in a stronger interaction between dislocations from different slip systems and, as a consequence, in stronger work hardening. Therefore, [110] tensile creep may eventually yield higher creep rates as compared to creep in the [001] direction. In Reference 20, we used TEM diffraction contrast to identify specific dislocation reactions in the $\gamma$ channels associated with shear creep deformation of CMSX-6. We have shown that not all of the slip systems with the same external Schmid factor are actually activated. We have also discussed which additional factors (coherency stress fields in the $\gamma/\gamma'$ microstructure, stress fields of other dislocations, or formation of dislocation networks around $\gamma'$ cubes) need to be considered when interpreting the deformation rates of superalloy single crystals. We have also considered the possible role of a cutting

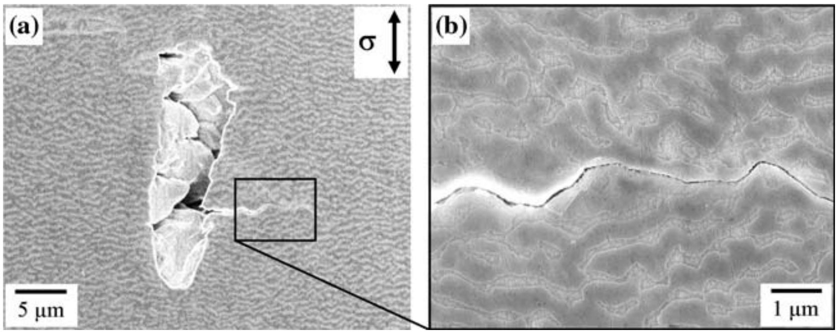

Fig. 16—SEM micrographs from a [001] sample crept at 1293 K and 240 MPa for 25 h (after polishing and etching): (*a*) overview and (*b*) microcrack grows along $\gamma/\gamma'$ interfaces.

process, where two $\gamma$-channel dislocations with different Burgers vectors jointly shear the $\gamma'$ phase.[26,27] Figure 11(a) shows $\gamma$-channel dislocations such as those that were observed in Reference 20, and Figure 11(b) shows a $\gamma'$ cutting event such as those observed and discussed in References 26 and 27. Our microstructural results on the role of dislocations during high temperature and low stress creep are in line with the microstructural scenarios that we described earlier.[20,26,27] This also holds for the observation of rafting in Figure 8, which occurs in all $\gamma/\gamma'$ microstructures in negative misfit superalloy single crystals.[33,36,38]

Two new results were obtained in the present study. First, it is very interesting to note that the slope of the $\log \dot{\varepsilon}(\varepsilon)$ creep curves of the [110] creep tests is significantly steeper than that of the [001] specimens (Figure 5). Figure 6 proves that these slopes are not affected by the presence/absence of aligned porosity for creep strains up to 10 pct. We conclude that microstructural softening is more pronounced in [110] than in [100] or [111] tensile creep. This may have to do with different thermodynamic or kinetic conditions for the coarsening of the $\gamma'$ phase in different tensile creep directions. Work is presently under way to clarify this effect. Second, we have been able to show that the presence of aligned cast pores strongly affects the deformation and failure characteristics in the later stages of creep. The presence of cast pores that line up parallel to the direction of the primary dendrites (Figures 1(a) and 12(b)) results in an earlier onset of rapid tertiary creep and in lower rupture strains in the [100] and [110] directions (with aligned cast pores perpendicular to the direction of the applied stress) than in the [001] and [101] directions, where cast porosity is not aligned perpendicular to the direction of the applied stress. The results from Figure 6 clearly document that mechanical anisotropy of single-crystal Ni-base superalloys is not only related to dislocation processes. Aligned cast micropores can also independently contribute to creep anisotropy in affecting the onset of tertiary creep and the corresponding rupture strains. Figure 18 schematically illustrates the alignment of cast pores in tensile creep specimens, which we used to characterize the three crystallographic directions, [001], [110], and [111]. From Figure 18, it is clear why [110] specimens show the earliest onset of tertiary creep and the lowest rupture strains.

Link *et al.*[52] recently showed how synchrotron X-ray tomography can be used to obtain information on the three-dimensional distribution of pores. They investigated the superalloys CMSX-6, SRR99, CMSX-4, and CMSX-10 and found pre-existing large pores that correspond to our interdendritic cast micropores. They also

**Table III Creep Behavior of Different Single-Crystal Superalloys in Terms of Stress Exponents $n$ and Apparent Activation Energies $Q_{app}$ from the Creep Equation $\dot{\varepsilon} = C \cdot \exp(-Q_{app}/RT) \cdot \sigma^n$ as Reported in the Literature**

| Temperature Range (K) | Stress Range (MPa) | $n$ | $Q_{app}$ (kJ/mole) | Type of Test (T = Tensile Test) | Material | Reference |
|---|---|---|---|---|---|---|
| 1293 | 160 to 240 | 4.6 | — | [001]T | LEK 94 | present study |
| 1293 | 160 to 240 | 5.6 | — | [110]T | LEK 94 | present study |
| 1293 | 160 to 240 | 5.3 | — | [111]T | LEK 94 | present study |
| 1253 to 1323 | 200 | — | 477 | [001]T | LEK 94 | present study |
| 1253 to 1323 | 200 | — | 531 | [110]T | LEK 94 | present study |
| 1253 to 1323 | 200 | — | 482 | [111]T | LEK 94 | present study |
| 1073 to 1173 | 450 to 650 | 7.0 | 495 | [001]T | CMSX-3 | 15 |
| 1023 to 1223 | 120 to 490 | 10.0 to 12.0 | 565 ± 42 | [001]T | Early $\gamma/\gamma'$ alloy | 10 |
| 1200 to 1311 | 140 to 310 | 10.0 ± 0.7 | 475 ± 109 | [001]T | Ni-Al-Mo-Ta | 47 |
| 1123 to 1223 | 180 to 490 | 7.0 | 510 | [001]T | SRR 99 | 48 |
| 1023 to 1253 | — | 7.0 to 13.0 | 507 | [001]T | SRR 99 | 49 |
| 1223 to 1373 | 301 | — | 670 | [001]T | CMSX-4 | 37 |
| 1073 to 1223 | 654 | — | 475 | [001]T | CMSX-4 | 37 |
| 1073 to 1373 | 80 to 900 | 7.2 to 13.5 | — | [001]T | CMSX-4 | 37 |
| 1293 to 1373 | 100 | — | 504 to 566 | shear* | CMSX-4 | 25 |

*Shear creep tests on the macroscopic crystallographic shear systems: $\{001\} <110>$ and $\{001\} <01\bar{1}>$.

Table IV. Schmid Factors of {111} < 110 > Glide Systems for Load in [001], [110], and [111] Tensile Directions

| Glide System | Glide Plane | Burgers Vector | Schmid factor [001] | Schmid factor [110] | Schmid factor [111] |
|---|---|---|---|---|---|
| 1 | $(111)$ | $[\bar{1}10]$ | 0 | 0 | 0 |
| 2 | $(111)$ | $[0\bar{1}1]$ | 0.408 | 0.408 | 0 |
| 3 | $(111)$ | $[10\bar{1}]$ | 0.408 | 0.408 | 0 |
| 4 | $(\bar{1}11)$ | $[\bar{1}\bar{1}0]$ | 0 | 0 | 0.272 |
| 5 | $(\bar{1}11)$ | $[101]$ | 0.408 | 0 | 0.272 |
| 6 | $(\bar{1}11)$ | $[01\bar{1}]$ | 0.408 | 0 | 0 |
| 7 | $(\bar{1}\bar{1}1)$ | $[1\bar{1}0]$ | 0 | 0 | 0 |
| 8 | $(\bar{1}\bar{1}1)$ | $[011]$ | 0.408 | 0.408 | 0.272 |
| 9 | $(\bar{1}\bar{1}1)$ | $[\bar{1}0\bar{1}]$ | 0.408 | 0.408 | 0.272 |
| 10 | $(1\bar{1}1)$ | $[110]$ | 0 | 0 | 0.272 |
| 11 | $(1\bar{1}1)$ | $[\bar{1}01]$ | 0.408 | 0 | 0 |
| 12 | $(1\bar{1}1)$ | $[0\bar{1}\bar{1}]$ | 0.408 | 0 | 0.272 |

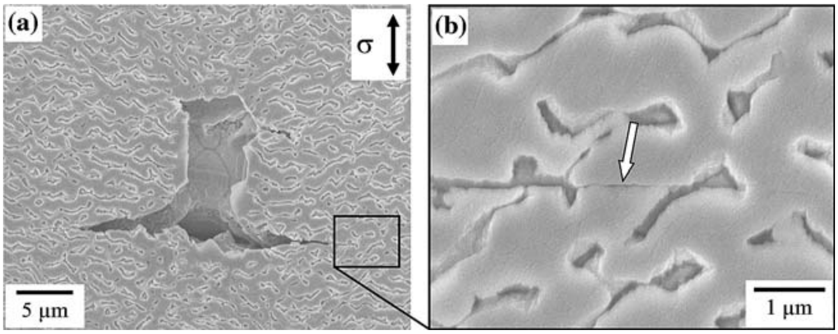

Fig. 17—SEM micrographs from a [001] sample crept at 1293 K and 160 MPa for 193 h (after polishing and etching): (*a*) overview and (*b*) microcrack propagates through $\gamma'$ rafts.

showed that new, significantly smaller pores form during 1100 °C creep in all parts of the microstructure. These small pores could not be detected in the present work using SEM. They are homogeneously distributed[52] and therefore do not contribute to the type of anisotropic creep damage accumulation reported in the present study. More insight can probably be gained by using synchrotron X-ray tomography to study the evolution of porosity during < 110 > and < 111 > tensile creep.

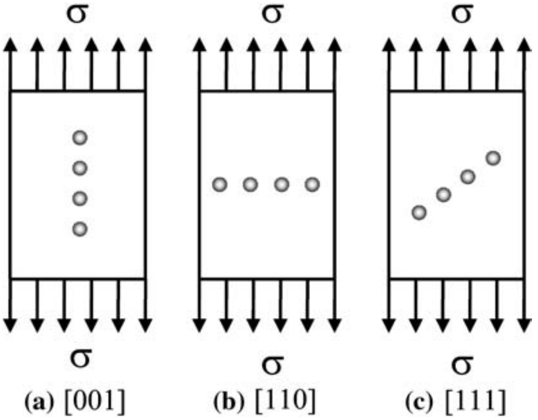

Fig. 18—Schematic illustration of the alignment of interdendritic pores with respect to the applied stress in (*a*) [001], (*b*) [110], and (*c*) [111] specimens.

The SEM micrographs such as those shown in Figures 14 through 17 suggest that tertiary creep and rupture is associated with the nucleation and growth of microcracks from pre-existing cast micropores. In the case of [110] specimens, it is easiest for such microcracks to link up, increasing the stress in the remaining undamaged cross section and leading to rupture. On the other hand, our results show that under the stress and temperature conditions considered in the present study, the cracks initiating from cast micropores only negatively affect creep behavior for strains exceeding 10 pct. This allows exclusion of the possibility that dendritic segregation contributes to the creep rupture anisotropy observed in the present study.

Microcracks that emanate from cast micropores were observed to follow $\gamma/\gamma'$ interfaces at a higher stress and lower degree of rafting (Figure 16), while they propagate through a $\gamma'$ region at a lower stress and a higher degree of rafting (Figure 17). Further work on the statistical importance of these crack path scenarios is required to clarify this observation, which may well be related to the specific three-dimensional morphologies of the $\gamma/\gamma'$ environments of the microcracks and to the contiguity of the $\gamma'$ phase.

Our study clearly demonstrates that microcrack initiation and growth from pre-existing cast micropores is important. Further work is required to study this phenomenon.

## V. SUMMARY AND CONCLUSIONS

In the present study, we use miniature creep specimens to study mechanical and microstructural aspects of short-term creep of the single-crystal superalloy LEK 94 in the 1000 °C temperature range. Our results can be summarized as follows.

1. Tensile creep experiments were performed on samples oriented in the [001], [110], and [111] crystallographic directions. Creep curves in the form of a logarithm of strain rate *vs* strain reveal no evidence of a steady state or minimum strain rate. Rather, the strain rate slowly accelerates toward tertiary creep and final failure. The creep data obtained from the miniature creep samples for the secondary and tertiary creep regimes are in good agreement with data from full size standard samples.
2. The temperature and stress dependence of the creep rate at 5 pct strain has been determined for three crystallographic directions. Stress exponents with values of 4.6 ([001]), 5.6 ([110]), and 5.3 ([111]) were obtained. For apparent activation energies of creep, values of 477 kJ/mole ([001] direction), 531 kJ/mole ([110] direction), and 482 kJ/mole ([111] direction) were found. These values are in good agreement with what was observed for other Ni-base superalloy single crystals. The values found for the apparent activation energy of creep are high, and it remains to be proven that they can be rationalized by a simple diffusion process. The stress exponents are too high to allow an interpretation of creep on the basis of a steady-state creep scenario. The temperature and stress dependence of creep is not strongly affected by crystallography.
3. In contrast, the creep resistance depends on the crystallographic direction in tensile creep testing, and [111] specimens show the lowest and the [110] specimens the highest creep rates. This can be explained using a combined argument involving the values of Schmid factors (the higher, the faster) and the number of activated slip systems (the more, the slower in the later stages of creep).
4. High temperature and low stress creep of LEK 94 is associated with a number of microstructural processes, including dislocation plasticity in the $\gamma$ channels and in the $\gamma'$ phase, rafting of the $\gamma'$ phase, and the nucleation and growth of microcracks from preexisting cast micropores.
5. Dislocation plasticity and rafting in LEK 94 occurs in very much the same way as previously described for other negative misfit single-crystal superalloys. Our results suggest that softening processes (not related to damage accumulation) show a dependence on the direction of creep loading. Further work is required to study this point.
6. As a striking new result, it was observed that aligned cast micropores can have a significant effect on the onset of tertiary creep and on rupture strains. In crystallographic tensile creep directions perpendicular to the direction of the alignment of pre-existing cast micropores, we observe an early onset of rapid tertiary creep and small rupture strains.

## ACKNOWLEDGMENT

The authors acknowledge funding by the Deutsche Forschungsgemeinschaft (DFG) under Contract No. EG 101/9.

## REFERENCES

1. B.H. Kear, S.M. Copley, and B.J. Piearcey: *Proc. 6th Int. Congr. for Electron Microscopy*, (Nihnbashi Ltd, Kyoto, 1966) 397–98.
2. C.T. Sims: in *Superalloys 1984*, Maurice Gell et al., eds., TMS, Warrendale, PA, 1984, pp. 399–419.
3. D.D. Pearson, R.D. Lemkey, and B.H. Kear: in *Superalloys 1980*, Proc. 4th Int. Symp. on Superalloys, ASM, Metals Park, OH, 1980, p. 513.
4. M. McLean: *Directionally Solidified Materials for High Temperature Service*, (The Metals Society, London, 1983).
5. M.V. Nathal, R.A. MacKay, and R.V. Miner: *Metall. Trans. A*, 1989, vol. 20A, pp. 133–41.
6. M. Kolbe, J. Murken, D. Pistolek, G. Eggeler, and H.-J. Klam: *Mat.-wiss Werkstofftech.*, 1999, vol. 30, pp. 465–72.
7. J. Murken, K. Serin, and G. Eggeler: Proc. Baltica V—*Int. Conf. on Cond. Life Managem. Power Plants*, S. Hietanen and P. Auerkari, eds., VTT Technical Research Centre of Finland, Espoo, 2001, vol. 2, pp. 583–91.
8. G. Mälzer, A. Kostka, G. Eggeler, S. Reese, and T. Mack: *TMS Lett.*, 2005, vol. 2, pp. 27–28.
9. C. Carry and J.L. Strudel: *Acta Metall.*, 1977, vol. 25, pp. 767–77.
10. C. Carry and J.L. Strudel: *Acta Metall.*, 1978, vol. 26, pp. 859–70.
11. C. Carry, S. Dermarkar, J.L. Strudel, and B.C. Wonsiewicz: *Metall. Trans. A*, 1979, vol. 10A, pp. 855–60.
12. M. Feller-Kniepmeier and T. Link: *Z. Metallkd.*, 1985, vol. 76, pp. 283–87.
13. M. Feller-Kniepmeier and T. Link: *Metall. Trans. A*, 1989, vol. 20A, pp. 1233–38.
14. B. Decamps, A. Morton, and M. Condat: *Phil. Mag.*, 1991, vol. 64, pp. 641–68.
15. T. Pollock and A.S. Argon: *Acta Metall. Mater., 1992*, 1992, vol. 40, pp. 1–30.
16. U. Glatzel: *Microstructure and Internal Strains of Undeformed and Creep Deformed Samples of a Nickel-Base Superalloy (Habilitationsschrift)*, (Verlag Dr. Köster, Berlin, 1994).
17. M. Benyoucef, N. Clement, and A. Coujou: *Phil. Mag.*, 1995, vol. 72, pp. 1043–56.
18. H. Mughrabi, H. Feng, and H. Biermann: *Proc. IUTAM Symp. Held at Sèvres*, A. Pineau and A. Zaoui, eds., Kluwer Academic Publishers, Dordrecht, 1996.
19. F.R.N. Nabarro and H.L. Villiers: *The Physics of Creep*, (Taylor & Francis, London, 1995).
20. C. Mayr, G. Eggeler, and A. Dlouhy: *Mater. Sci. Eng.*, 1996, vol. A207, pp. 51–63.
21. M. Probst-Hein, A. Dlouhy, and G. Eggeler: *Acta Mater.*, 1999, vol. 47, pp. 2497–2510.
22. Z. Peng, U. Glatzel, T. Link, and M. Feller-Kniepmeier: *Scripta Mater.*, 1996, vol. 34, pp. 221–26.
23. M. Veron, Y. Brechet, and F. Louchet: in *Superalloys 1996*, R.D. Kissinger et al., eds., TMS, Warrendale, 1996, pp. 181–90.
24. M. Kamaraj, C. Mayr, M. Kolbe, and G. Eggeler: *Scripta Mater.*, 1998, vol. 38, pp. 589–94.
25. M. Kamaraj, K. Neuking, M. Kolbe, and G. Eggeler: *Materials for Advanced Power Engineering*, Proc. 6th Liege Conf., Part II, J. Lecomte-Beckers *et al.*, eds., Schriften des Forschungszentrum Jülich, Reihe Energietechnik/Energy Technology, Jülich, 1998, vol. 5.
26. G. Eggeler and A. Dlouhy: *Acta Mater.*, 1997, vol. 45, pp. 4251–62.

27. R. Srinivasan, G. Eggeler, and M.J. Mills: *Acta Mater.*, 2000, vol. 48, pp. 4867–78.
28. A. Kostka, G. Mälzer, G. Eggeler, A. Dlouhy, S. Reese, and T. Mack: *J. Mater. Sci.*, 2006, in press.
29. J.X. Zhang, H. Harada, and Y. Koizumi: *J. Mater. Res.*, 2006, vol. 21, pp. 647–54.
30. S.H. Ai, V. Lupinc, and M. Maldini: *Scripta Metall. Mater.*, 1992, vol. 26, pp. 579–84.
31. A.H. Sherry and R. Pilkington: *Mater. Sci. Eng.*, 1993, vol. A 172, pp. 51–61.
32. A.M. Hashem, D. Goldschmidt, and E. El-Magd: *Mat.-wiss. Werkstofftech.*, 1994, vol. 25, pp. 133–38.
33. N. Matan, D.C. Cox, C.M.F. Rae, and R.C. Reed: *Acta Mater.*, 1999, vol. 47, pp. 2031–45.
34. A. Fredholm and J.L. Strudel: *High Temperature Alloys, Their Exploitable Potential*, Proc. Petten. Int. Conf., 1985, J.B. Mariott, H. Herz, J. Nihoul, and J. Ward, eds., Elsevier Applied Science, London,1987, pp. 9–18.
35. A. Epishin, T. Link, U. Brückner, and P.D. Portella: *Acta Mater.*, 2001, vol. 49, pp. 4017–23.
36. K. Serin, R.D. Neuser, G. Eggeler, M. Kamaraj, M. Kolbe, and M. Heitkemper: *Prakt. Metallogr.*, 2001, vol. 38, pp. 680–98.
37. W. Schneider: Ph.D. Thesis, Universität Erlangen-Nürnberg, Nürnberg, 1993.
38. K. Serin, G. Göbenli, and G. Eggeler: *Mater. Sci. Eng.*, 2004, vol. A387–A389, pp. 133–37.
39. M. Kolbe, A. Dlouhy, and G. Eggeler: *Mater. Sci. Eng.*, 1998, vol. A 246, pp. 133–42.
40. G.K. Bouse and J.R. Mihalisin: in *Superalloys, Supercomposites and Superceramics*, J.K. Tien and T. Caulfield, in *Materials Science and Technology Series*, A.S. Nowick and G.G. Libowitz, eds., Academic Press, Inc., San Diego, CA, 1989.
41. H. Riedel: *Fracture at High Temperatures*, (Springer-Verlag, Berlin, 1987).
42. G. Eggeler, J.C. Earthman, N. Nilsvang, and B. Ilschner: *Acta Metall.*, 1989, vol. 37, pp. 49–60.
43. G. Eggeler: *Acta Metall. Mater.*, 1991, vol. 39, pp. 221–31.
44. G. Mälzer: Ph.D. Thesis, Ruhr-Universität Bochum, Bochum, 2007.
45. R.W. Evans and B. Wilshire: *Creep of Metals and Alloys*, (Institute of Metals, London, 1985).
46. B. Ilschner: *Hochtemperatur-Plastizität*, (Springer-Verlag, Berlin, 1973).
47. R.A. MacKay and L.J. Ebert: *Metall. Trans. A*, 1985, vol. 16A, pp. 1969–82.
48. M. Maldini and V. Lupinc: *Scripta Metall.*, 1988, vol. 22, pp. 1737–41.
49. R. Wege and J. Wortmann: *Mat.-wiss. Werkstofftech.*, 1989, vol. 20, pp. 207–16.
50. H. Bakker: *Phys. Status Solidi*, 1968, vol. 28, pp. 569–76.
51. G.F. Hancock: *Phys. Status Solidi (a)*, 1971, vol. 7, pp. 535–40.
52. T. Link, S. Zabler, A. Epishin, A. Haibel, M. Bansal X. Thibault: *Mater. Sci. Eng.*, 2006, vol. A425, pp. 47–54.